Acta Cryst B
STRUCTURAL SCIENCE
CRYSTAL ENGINEERING
MATERIALS

ISSN 2052-5206

The atacamite family of minerals – a testbed for quantum spin liquids

Thomas Malcherek,[a] Mark D. Welch[b] and Peter A. Williams[c]

[a]Mineralogisch-Petrographisches Institut, Fachbereich Geowissenschaften, Universität Hamburg, Grindelallee 48, 20146 Hamburg, Germany, [b]Department of Earth Sciences, Natural History Museum, London, SW7 5BD, UK, and [c]Western Sydney University, Dean's Unit, School of Science and Health, Locked Bag 1797, Penrith, NSW 2751, Australia

Received 16 July 2018
Accepted 30 November 2018

Edited by J. Lipkowski, Polish Academy of Sciences, Poland

Keywords: Jahn–Teller distortion; spin liquid; geometric frustration; herbertsmithite; paratacamite; clinoatacamite.

Polymorphism of $Cu_2(OH)_3Cl$ coupled with partial substitution of Jahn–Teller active Cu^{2+} by other divalent metal cations gives rise to the complex mineralogy of the atacamite family of secondary basic copper chlorides. Herbertsmithite, $Cu_3Zn(OH)_6Cl_2$, in which Zn substitutes for one quarter of the Cu atoms, provides a lattice of corner-sharing triangles of paramagnetic Cu^{2+} (spin $\frac{1}{2}$) cations, rendering the mineral a perfect realization of a kagome antiferromagnet. Geometric frustration of conventional antiferromagnetism is expected to give rise to exotic ground states, with dynamic magnetic structures that might turn out to be physical realizations of quantum spin liquids. In this paper, a synopsis of the key topological, compositional and behavioural features of minerals in the atacamite family is given, with emphasis on the kagome character of the resulting lattice of Cu^{2+} cations.

1. Introduction

Atacamite, of composition $Cu_2(OH)_3Cl$, is the most common of a group of minerals closely related in composition and crystal structure. These secondary copper minerals occur in the oxidation zone of metal ores in arid environments and as corrosion products of copper and its alloys. They have also been used as green pigments, though it is not always clear whether their occurrence in paintings is of a primary or secondary nature (Scott, 2000).

The recent discovery of several new atacamite-group minerals attests to the complex polymorphism that is controlled both by chemistry and by Jahn–Teller (JT) distortions.

One of these recently described mineral species, herbertsmithite, $Cu_3Zn(OH)_6Cl_2$, was synthesized and examined for its low-temperature magnetic properties (Shores *et al.*, 2005) soon after its first description in the mineralogical literature (Braithwaite *et al.*, 2004). In herbertsmithite the Cu^{2+} cations occupy the nodes of a kagome lattice, a two-dimensional lattice composed of corner-sharing triangles. A perfect experimental realization of such a lattice, with its nodes occupied by antiferromagnetically interacting magnetic moments, has been long sought after. Due to geometric frustration of conventional Néel states of antiferromagnetic order, various forms of spin liquids have been predicted for such a two-dimensional lattice (Mendels & Bert, 2010; Zhou *et al.*, 2017).

This article focuses on the structural relations between the various mineral species and polymorphs found in the atacamite family. A common feature of these minerals is the occurrence of layers containing triangular arrangements of Cu^{2+} cations, while the interlayer bonding, as well as the

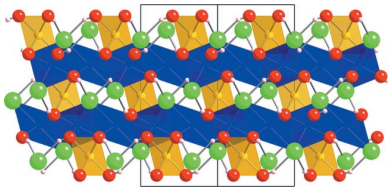

coordination of the Cu cations, vary. We shall see how the intricacies of the Cu coordination chemistry in the atacamite family affect the topological realization of an ideal kagome lattice as a host structure for unusual magnetic properties. Earlier reviews of the subject (Mendels & Bert, 2016; Norman, 2016) have concentrated on the known magnetic properties of herbertsmithite. The physics of quantum spin liquids has been reviewed elsewhere (Balents, 2010; Zhou *et al.*, 2017).

1.1. Geometric frustration

As the Cu^{2+} cation carries a single unpaired electron ($S = \frac{1}{2}$), it provides an ideal carrier for magnetic moments in realizations of theoretical spin systems. A triangular arrangement of antiferromagnetically coupled (Ising) spins cannot satisfy all interactions simultaneously. If two spins are already in antiparallel orientation, the third cannot be antiparallel to both of them. The situation is more complex for Heisenberg spins with arbitrary orientation (Norman, 2016), but especially two-dimensional lattices of corner-sharing triangles are expected to give rise to geometric frustration of ordered Néel states, thus requiring other ground states with either fluctuating spins or more complex ordering patterns. In a quantum spin liquid the spins would fluctuate even at 0 K. While the magnetic moments would correlate, there would be no static magnetic order attributable to them.

Several structural requirements can be postulated in order to obtain a perfect kagome antiferromagnet with Cu^{2+} cations as a carrier of magnetic moments: (i) the lattice topology should provide an undistorted and undiluted representation of a kagome lattice (ii) the Cu-ligand positions should enable sufficiently strong and constant antiferromagnetic coupling and (iii) the kagome layers should be magnetically isolated in the third dimension.

The nature of the spin coupling is determined by the magnetic superexchange between the Cu^{2+} cations. This is primarily determined by the bond angle between two given Cu^{2+} cations and their bridging oxygen anion. In the basic copper chlorides the Cu—O(H) bonds are the shortest and the coupling character is therefore dominated by the Cu—O—Cu bridging angles. The expected superexchange coupling has been discussed previously (Lee *et al.*, 2007; Wills & Henry, 2008; Freedman *et al.*, 2010). For bridging angles at and above 120° the coupling should be antiferromagnetic, with the strength of the antiferromagnetic coupling increasing as the angle approaches 180°. For bridging angles between 90° and 120° the situation appears to be less clear, but as pointed out by Wills & Henry (2008), an appreciable degree of ferromagnetic coupling is expected to be present for angles between 91° and 102°. For herbertsmithite the crucial Cu—O—Cu angles within the kagome layers are close to 120°, whereas potential Cu—O—Cu bridges branching out to interlayer sites have angles close to 96°. Thus antiferromagnetic coupling is indeed expected for the kagome layers, while ferromagnetic coupling among different layers could play a role if Cu^{2+} cations reside on interlayer sites.

2. The copper end members: atacamite, botallackite and clinoatacamite

Atacamite is orthorhombic with space group *Pnma*. The crystal structure of atacamite is shown in Figs. 1(*a*) and 1(*c*). The topological similarity between atacamite and spinel structures of general composition AB_2O_4 has been pointed out by Parise & Hyde (1986). In this structural analogy, the AO_4 tetrahedra of the spinel structure are replaced by $Cl(HO)_3$ tetrahedra with a vacant centre. The three hydrogen atoms located on the edges of the tetrahedron effectively substitute for the *A* cation at the centre. The positions of the Cu^{2+} cations in atacamite represent the topology of the *B* cations in the spinel structure. The *B* cations form a three-dimensional network of corner-sharing tetrahedra, as is also found in the pyrochlore structure. The spinel and pyrochlore lattices of paramagnetic *B* atoms have themselves been studied for frustrated antiferromagnetism in a large variety of compounds (Lee *et al.*, 2010). Pyrochlores $R_2Ti_2O_7$, where *R* is a paramagnetic rare-earth element, are well known for their 'spin-ice' formation (Bramwell & Gingras, 2001; Balents, 2010; Castelnovo *et al.*, 2012). However, atacamite transforms to an ordered antiferromagnetic state at a Néel temperature of 9 K as shown by Zheng *et al.* (2005) (Table 1). It involves a distorted pyrochlore lattice of paramagnetic Cu^{2+} cations with a mixed ligand coordination of $(OH)^-$ and Cl^- anions. The $Cu(OH)_4Cl_2$ coordination consisting of four equatorial OH groups and two *trans*-oriented Cl atoms forming an elongated octahedron is found in all minerals of the atacamite family. These polyhedra form edge-sharing chains extending parallel to [010] in atacamite [Fig. 1(*a*)]. In contrast to this, the additional $Cu(OH)_5Cl$ coordination environment is characteristic

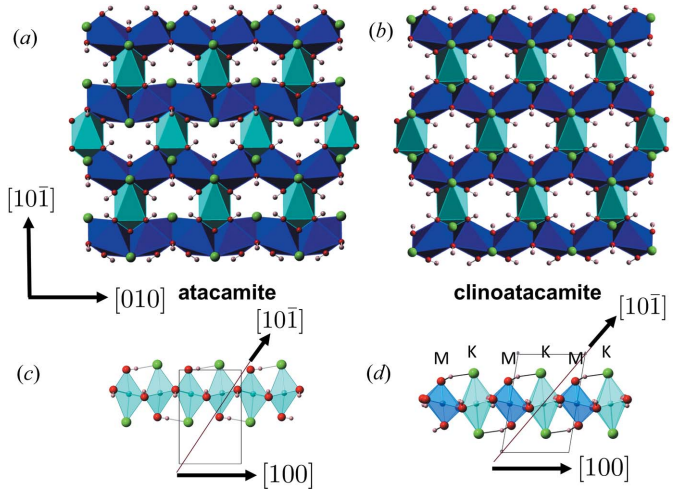

Figure 1
The (101) polyhedral sheets of atacamite (*a*) and clinoatacamite (*b*). In clinoatacamite all polyhedra are $Cu(OH)_4Cl_2$, whereas in atacamite $Cu(OH)_5Cl$ polyhedra are also present [teal coloured in (*a*)]. The Cl position in $Cu(OH)_5Cl$ polyhedra alternates along the [100] direction in atacamite (*c*), while in clinoatacamite, $Cu(OH)_4Cl_2$ polyhedra (*K*) alternate with $Cu(OH)_6$ polyhedra (*M*) along this direction (*d*). Oxygen atoms are shown in red, Cl atoms in green and Cu in shades of blue, indicating site equivalence. The smallest spheres represent hydrogen atoms.

Table 1
Cu-containing minerals of the atacamite family and related mineral phases, their composition, space-group symmetry, normalized cell volume and known transition temperatures to various magnetic phases.

AF = antiferromagnetic, CF = canted ferromagnetic, FM = ferromagnetic, SG = spin glass.

Mineral	Chemical formula	Space group	System	V/Z (Å^3)	T_c (K)	Reference
Atacamite	$Cu_2(OH)_3Cl$	*Pnma*	Orthorhombic	94	9.0, AF	Parise & Hyde (1986); Zheng *et al.* (2005)
Clinoatacamite	$Cu_2(OH)_3Cl$	$P2_1/n$	Monoclinic	94	6, CF	Wills & Henry (2008)
Botallackite	$Cu_2(OH)_3Cl$	$P2_1/m$	Monoclinic	99	7.2, AF	Zheng *et al.* (2005)
Iyoite	$CuMn(OH)_3Cl$	$P2_1/m$	Monoclinic	106	n.d.	Nishio-hamane *et al.* (2017)
Paratacamite	$Cu_3(Cu,Zn)(OH)_6Cl_2$	$R\bar{3}$	Trigonal	189	n.d.	See text
Herbertsmithite	$Cu_3Zn(OH)_6Cl_2$	$R\bar{3}m$	Trigonal	188	–	See text
Tondiite	$Cu_3Mg(OH)_6Cl_2$	$R\bar{3}m$	Trigonal	189	4–5, FM	Colman *et al.* (2011)
Leverettite	$Cu_3Co(OH)_6Cl_2$	$R\bar{3}m$	Trigonal	190	3.5, SG	Kampf *et al.* (2013*b*); Li & Zhang (2013)
Gillardite	$Cu_3Ni(OH)_6Cl_2$	$R\bar{3}m$	Trigonal	187	6, SG	Li & Zhang (2013)
Kapellasite	$Cu_3Zn(OH)_6Cl_2$	$P\bar{3}m1$	Trigonal	197	–	Kermarrec *et al.* (2014)
Haydeeite	$Cu_3Mg(OH)_6Cl_2$	$P\bar{3}m1$	Trigonal	196	4.2, FM	Boldrin *et al.* (2015)
Misakiite	$Cu_3Mn(OH)_6Cl_2$	$P\bar{3}m1$	Trigonal	203	n.d.	Nishio-hamane *et al.* (2017)

for atacamite and botallackite. In atacamite these coordination polyhedra form edge-sharing chains with alternating position of the apical Cl atom along the [100] direction (Fig. 1*c*).

The crystal structure of clinoatacamite [Figs. 1(*b*) and 1(*d*)] can be derived from that of atacamite by locally interchanging the Cu ligand atoms, thus keeping the $Cu_2(OH)_3Cl$ stoichiometry. Swapping neighbouring OH groups and Cl atoms between two adjacent $Cu(OH)_5Cl$ octahedra along the [100] chains [Figs. 1(*c*) and 1(*d*)] results in elongated $Cu(OH)_4Cl_2$ octahedra alternating with JT-distorted $Cu(OH)_6$ octahedra [*K* and *M*, respectively, in Fig. 1(*d*)]. Together with the other $Cu(OH)_4Cl_2$ elongated octahedron that already exists in the atacamite structure, three symmetrically inequivalent Cu sites result in clinoatacamite. While the elongated *K*-octahedra form distorted kagome layers of corner-sharing Cu triangles normal to [201], the (4 + 2) JT-distorted *M*-octahedra occupy the space between these layers (interlayer sites). Epitaxial growth of clinoatacamite on atacamite crystals has been observed in some cases (Malcherek *et al.*, 2017). Clinoatacamite was described only in 1996 (Grice *et al.*, 1996; Jambor *et al.*, 1996). Prior to that, the mineral had often been identified as paratacamite and references to paratacamite in older literature might actually refer to clinoatacamite.

Botallackite (Hawthorne, 1985), as the third polymorph of $Cu_2(OH)_3Cl$, has a layered structure. Each layer is composed of alternating chains of $Cu(OH)_5Cl$ and $Cu(OH)_4Cl_2$ polyhedra that can also be found in the atacamite crystal structure. While these chains have perpendicular direction in atacamite [Figs. 1(*a*) and 1(*c*)], they are parallel in botallackite, laterally connected by shared OH groups. The layers formed in this way are linked only by relatively weak O—H···Cl hydrogen bonding. In contrast to atacamite, the Cu^{2+} ions form layers of edge-sharing triangles in botallackite. Recently a Zn-substituted botallackite has been described (Yang *et al.*, 2016) as a copper corrosion product, where Zn substitutes for Cu on all sites coordinated by five OH and one Cl. Iyoite is the Mn-substituted species isostructural with botallackite (Table 1). Botallackite is relatively rare in nature, but the formation of clinoatacamite and atacamite usually involves the intermediate formation of botallackite as a precursor (Pollard *et al.*, 1989; Krivovichev *et al.*, 2017).

3. The paratacamite group

Minerals of the paratacamite group have monoclinic ($P2_1/n$) or trigonal symmetry ($R\bar{3}$, $R\bar{3}m$). Their bond topology is identical to clinoatacamite, with the amount of monoclinic distortion determined by the cooperative Jahn–Teller effect related to Cu content. The structural differences between the different phases are minor and can best be distinguished experimentally by the presence or absence of characteristic superstructure diffraction maxima. In clinoatacamite, $Cu_2(OH)_3Cl$, replacement of Cu^{2+} by other divalent cations occurs preferentially at the interlayer site, *M*, that is coordinated by six OH groups. As the substituting divalent cations will, unlike Cu^{2+}, not generally cause a significant JT distortion

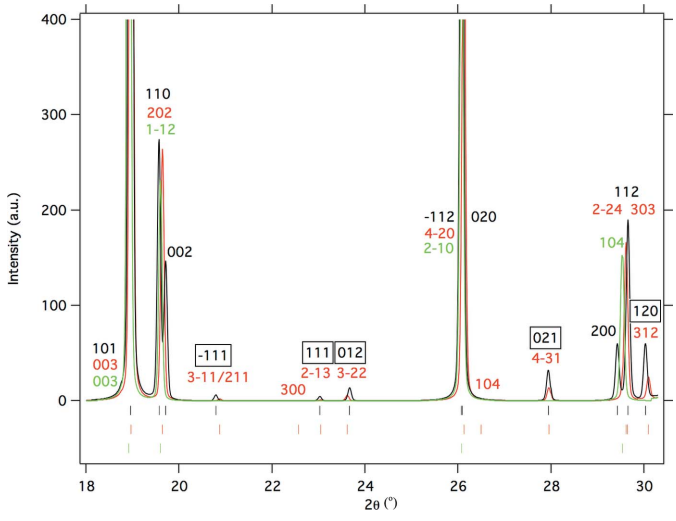

Figure 2
Simulated X-ray powder diffraction for clinoatacamite (black), paratacamite (red) and herbertsmithite (green) between 18 and 30.5° 2θ for Cu $K\alpha$ radiation (λ = 1.5418 Å), calculated from the respective crystal structures using *Jana2006* (Petříček *et al.*, 2014). Framed indices mark clinoatacamite superstructure reflections with $h + k + l = 2n + 1$.

of the coordination environment, the monoclinic distortion eventually disappears with increasing cation substitution. For Cu→Zn substitution the monoclinic to trigonal transformation has been observed between 6 and 9% Zn per formula unit (*pfu*) (Jambor *et al.*, 1996), the latter Zn content corresponding to a composition $Cu_3(Zn_{1/3}Cu_{2/3})(OH)_6Cl_2$.

The paratacamite structure has trigonal symmetry $R\bar{3}$ with two different interlayer positions, *M*1 and *M*2, and a superstructure that corresponds metrically to $2a_{\rm herb} \times 2a_{\rm herb} \times c_{\rm herb}$ (herb = herbertsmithite-type substructure). Fleet (1975) originally reported this superstructure for what he assumed to be paratacamite of end-member composition $Cu_2(OH)_3Cl$, as for atacamite. Later analysis of the sample material studied by Fleet confirmed that these crystals had a significant Zn content (Braithwaite *et al.*, 2004; Welch *et al.*, 2014). By studying paratacamite single crystals, it could also be shown that paratacamite transforms reversibly to the herbertsmithite structure type at elevated temperatures, marked by the disappearance and reappearance of the superstructure reflections (Welch *et al.*, 2014) (Fig. 2).

If all *M* sites have been substituted by Zn, the composition becomes $Cu_3Zn(OH)_6Cl_2$ and the space-group symmetry is $R\bar{3}m$. This is the mineral herbertsmithite (Braithwaite *et al.*, 2004), in which nominally the Cu^{2+} cations occupy all nodes of the kagome layers, while Zn cations occupy the interlayer *M* sites (Fig. 1*d*). The two inequivalent interlayer *M* sites of paratacamite (*M*1, *M*2) converge upon a single site in herbertsmithite that is coordinated by a regular antiprism of six oxygen atoms. While the kagome layers are distorted in clinoatacamite [Figs. 1(*b*) and 1(*d*)], they are perfectly regular in herbertsmithite, oriented normal to [001], which corresponds to the [201] direction of the clinoatacamite structure. Similarly, isostructural minerals with substituents other than Zn exist in the form of gillardite, $Cu_3Ni(OH)_6Cl_2$, leverettite, $Cu_3Co(OH)_6Cl_2$ and tondiite, $Cu_3Mg(OH)_6Cl_2$ (Table 1).

The herbertsmithite structure type is not restricted to compositions where this interlayer site is fully occupied by a cation that is not JT active, as the average regular antiprismatic coordination can result from the dynamic Jahn–Teller effect. This phenomenon is demonstrated by a reversible phase transition of pure $Cu_2(OH)_3Cl$ from the monoclinic clinoatacamite structure to the trigonal herbertsmithite structure at a temperature of 445 K (Malcherek *et al.*, 2017). The lattice distortion accompanying this transition to trigonal symmetry is relatively small, but the primitive unit cell of the resulting trigonal lattice is only half the size of that of clinoatacamite. Hence, the transition involves the disappearance of superlattice diffraction maxima that are characteristic of clinoatacamite (Malcherek & Schlüter, 2009; Malcherek *et al.*, 2017). The critical zone boundary position of the $R\bar{3}m$ parent symmetry is the *F* point of the $R\bar{3}m$ Brillouin zone and the primary distortion mode is F_{2+} with the largest displacement amplitudes observed for the oxygen atoms. In the $P2_1/n$ space group setting of clinoatacamite, the superstructure diffraction maxima that develop with the structural distortion have indices $h + k + l = 2n + 1$ (Fig. 2). These additional reflections are weaker than the fundamental reflections. As the monoclinic distortion is rather small, the shift of the clinoatacamite reflections with respect to the trigonal parent structure is not easy to detect. A detailed account of the merging of clinoatacamite twin reflections and the development of superstructure intensities as a function of temperature has been given by Malcherek *et al.* (2017), based on single crystal X-ray diffraction. As is evident from Fig. 2, reflections distinguishing the paratacamite reciprocal lattice from that of herbertsmithite are in close proximity to the clinoatacamite superstructure reflections but have even lesser intensity than the latter. Identification of the three polymorphs by conventional X-ray powder diffraction should therefore be extremely difficult.

The transformation of twinned clinoatacamite to paratacamite, followed by the already known transition to the herbertsmithite structure type has been described for Zn-free samples having minor Co and Ni substitution for Cu (Malcherek *et al.*, 2017). In contrast to this, pure clinoatacamite transforms directly to the herbertsmithite structure ($P2_1/n \leftrightarrow R\bar{3}m$) without this intermediate step and at higher temperatures than the Co- and Ni-bearing samples (445 K instead of ∼400 K; Malcherek *et al.*, 2017). The occurrence of displacive and reversible phase transitions between the polymorphs indicates that the paratacamite superstructure is a consequence of the cooperative Jahn–Teller effect, aided by the presence of non-JT active cations at the interlayer sites. The details will be discussed further in §4.

3.1. Herbertsmithite and its analogues

If the single interlayer site *M* of the herbertsmithite structure is completely occupied by diamagnetic Zn, the kagome layers should be magnetically isolated with respect to each other and the magnetic properties should be determined by the properties of the kagome layers. A voluminous literature on the magnetic properties of herbertsmithite now exists, since it was first described in 2004 [references cited by Norman (2016)]. It is known that herbertsmithite does not order magnetically down to 50 mK (Helton *et al.*, 2007; Mendels *et al.*, 2007), in spite of very large antiferromagnetic coupling of the magnetic moments, as indicated by a Curie–Weiss temperature in the order of −300 K and a calculated J_1 of 182 K (Jeschke *et al.*, 2013). No additional Bragg reflections indicative of a possible lattice distortion have been observed in synthetic herbertsmithite crystals down to temperatures of 2 K (Han *et al.*, 2011). Herbertsmithite displays a continuum of magnetic excitations at low temperatures – a hallmark of quantum spin liquids (Han *et al.*, 2012) – and no freezing of spins, not even into a glassy state. The dynamic antiferromagnetic correlations are weakly temperature dependent up to 120 K (de Vries *et al.*, 2009). Addition of more Cu leads to a frozen magnetic component for Zn contents of less than two-thirds at the interlayer site (Mendels *et al.*, 2007).

A complexity indicated by experiments on synthetic end-member herbertsmithite $Cu_3Zn(OH)_6Cl_2$ arises from Cu/Zn disorder between the interlayer site and kagome-layer sites, with a proportion of Cu residing at interlayer sites and a

corresponding amount of Zn at the kagome layers (Mendels & Bert, 2010; de Vries *et al.*, 2012). There is also evidence for non-stoichiometry ('off-composition' products) in synthetic herbertsmithite, with an excess of Cu^{2+} (Freedman *et al.*, 2010), potentially leading to ferromagnetic coupling between the kagome layers. By use of powder neutron diffraction, EXAFS and X-ray anomalous scattering, Freedman *et al.* (2010) detected no evidence for significant amounts of Zn entering the kagome layers. Other authors again report synthesis with an excess of Zn beyond the $Cu_3Zn(OH)_6Cl_2$ composition of herbertsmithite (de Vries *et al.*, 2012), suggesting that substantial amounts of Zn can enter the kagome sites.

Leverettite, $Cu_3Co(OH)_6Cl_2$, and gillardite, $Cu_3Ni(OH)_6Cl_2$, the Co^{2+} and Ni^{2+} analogues of herbertsmithite (Table 1) have also been synthesized (Li & Zhang, 2013). Unlike Zn, the interlayer cation in both compounds is not diamagnetic. At low temperatures a transition to a spin glass state has been observed in both minerals. In tondiite (Malcherek *et al.*, 2014), the Mg analogue of herbertsmithite, similar issues with Cu occupancy at interlayer sites exist as in herbertsmithite (Colman *et al.*, 2011; Kermarrec *et al.*, 2011). Known natural samples of tondiite have a maximum Mg content of 70% at the interlayer site. While there is no evidence of site disorder in the natural samples, synthetic tondiite with higher Mg concentrations (Colman *et al.*, 2011) appears to be susceptible to limited substitution of Mg atoms onto kagome sites, similar to the reported Zn substitution into the kagome layers of herbertsmithite. Site occupancy refinement of Mg versus Cu atoms is facilitated in tondiite, due to the high X-ray scattering contrast for this pair of elements. However, the limitations of the independent atom model should be kept in mind (Angel & Nestola, 2016), especially for the interpretation of X-ray powder diffraction data when small variations of site scattering are involved.

4. Paratacamite and the role of dynamic JT distortion

As mentioned above, two different interlayer Cu coordinations occur in the paratacamite crystal structure. Following the notation used by Welch *et al.* (2014), the *M*1 site has the same trigonal antiprismatic oxygen coordination as in herbertsmithite. The *M*2 site has an unusual (2 + 2 + 2) oxygen coordination, with opposing ligands at three distinct distances to *M*2, ranging between short (2.0 Å), intermediate (2.1 Å) and long (2.25 Å). Fig. 3(*a*) shows a section of the paratacamite structure, with the *M*1 interlayer site at its centre. The occurrence of the (2 + 2 + 2) distortion is usually attributed to the dynamic Jahn–Teller effect (Burns & Hawthorne, 1996), an interpretation that is supported by the strongly anisotropic displacement ellipsoids of oxygen observed in paratacamite (Welch *et al.*, 2014), [Fig. 3(*a*)]. The displacement ellipsoids are elongated in the Cu—O bond direction for most of the ligand oxygens of the *M*1$(OH)_6$ and the *M*2$(OH)_6$ polyhedra. The only exception is the O1 atom, which exhibits a smaller and more or less spherical atom displacement in comparison to the other three O atoms in the paratacamite structure. An O1—*M*2 bond length of about 2.0 Å at 300 K is the shortest of the (2 + 2 + 2) coordination environment of *M*2, and has been interpreted as the resultant effect of the superposition of only two of the three possible orientations of the JT-distorted CuO_6 octahedron, with O1—*M*2—O1 as the pivotal axis of the reorientation (Welch *et al.*, 2014).

Such a dynamic configuration may be the result of a cooperative JT effect with a short correlation length. To demonstrate this possibility, three identical clusters of clinoatacamite structure have been superimposed in Fig. 3(*b*), centred on an interlayer Cu cation. The three clusters differ only by a 120° rotation about the [201] direction, *i.e.* each cluster represents the orientation of the ordered structure of a twin domain of clinoatacamite. By superposition of the clusters the effect of dynamic switching between the three orientational states of an individual JT distortion and its cooperative effect on neighbouring Cu coordination environments can be simulated, assuming that the cooperative JT effect (Gehring & Gehring, 1975) is responsible for the macroscopic monoclinic distortion of the clinoatacamite structure. A similar approach was chosen by Malcherek *et al.* (2017), where the superposition of different oxygen ligand positions has been used to model qualitatively the experimentally obtained oxygen probability density functions. The same superposition of three different ligand positions can be observed at the centre of Fig. 3(*b*). This disorder of the ligand OH groups also gives rise to positional disorder of the Cu atoms in the kagome planes above and below the central interlayer position. For the central polyhedron (*M*1O_6) each Cu—O bond effectively is a time average of three different Cu–O pairs, yielding an average distance of approximately 2.12 Å.

For the nearest neighbour Cu atoms of *M*1 in the interlayer space, corresponding to *M*2 in the paratacamite structure (Fig. 3), these averages are different: the three differently oriented individual CuO_6 polyhedra yield bond averages resulting from (i) three short bonds of about 2 Å, (ii) one long

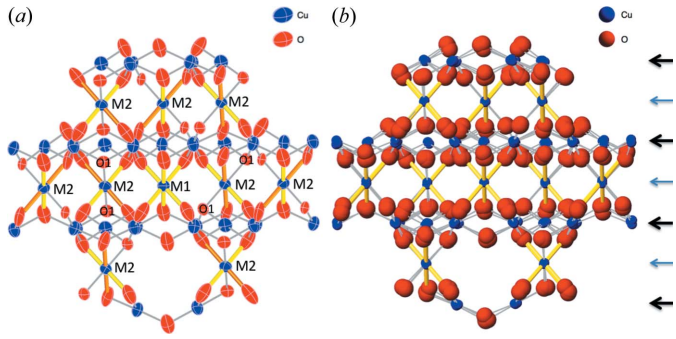

Figure 3
(*a*) Crystal structure of paratacamite, centred about the *M*1 position. [001] is pointing upwards. Long Cu—O bonds (2.25 Å) are shown in orange, intermediate Cu—O bonds (2.1 Å) in yellow and all other bonds as grey lines. (*b*) Superposition of three clusters of clinoatacamite crystal structure, rotated 0°, 120° and 240° about [201] (the upwards direction), with an interlayer Cu atom as their common centre. The longest Cu—O bonds (2.35 Å) in each cluster are shown in yellow. Arrows mark the position of interlayer cations (thin blue) and kagome layers (thick black). Cl and H atoms have been omitted in (*a*) and (*b*).

bond of 2.35 Å and two short bonds, and (iii) two long bonds and one short bond [long Cu—O bonds are coloured yellow in Fig. 3(*b*), so that average bonds resulting from case (ii) and (iii) appear in yellow, while average bonds resulting from case (i) appear in grey]. This essentially results in the (2 + 2 + 2) coordination described above.

It also confirms the interpretation of the nearly spherical and relatively small displacement parameters at the O1 position of paratacamite, because case (i) yields the uniquely short *M*2—O1 bond. Further comparison of Figs. 3(*a*) and 3(*b*) confirms that the (2 + 2 + 2) coordination seen at the *M*2 site of the paratacamite structure can be interpreted as a time average of the (4 + 2) polyhedral distortions observed in clinoatacamite. In particular, the direction of the longest *M*2—O bonds (orange) in paratacamite coincide with the case (iii) average, dominated by long Cu—O bonds, while shorter bonds [the yellow-coloured bonds in Fig. 3(*a*)] result for case (ii) averages. Also the size and shape of the refined displacement ellipsoids in paratacamite (Fig. 3*a*) are in good agreement with the outline of overlapping spheres obtained from the three differently oriented clinoatacamite clusters (Fig. 3*b*).

That the averaged bond length from the superposition of rotated clinoatacamite clusters matches the actual bond length in paratacamite, demonstrates that the paratacamite phase is a result of short-range cooperative JT displacement. The chosen rotation angles match those of the warped 'Mexican hat' potential governing the dynamic JT effect at the central Cu atom (Burns & Hawthorne, 1996). If the correlation length increases, the dynamic JT distortions 'lock' into the monoclinic distortion of a clinoatacamite twin domain. This is observed for temperatures below 370 K in the Co/Ni-doped samples studied by Malcherek *et al.* (2017). On the other hand, if the correlation length decreases even further, the dynamically JT distorted octahedra become independent – the cooperative JT distortion 'melts' – and the herbertsmithite type develops. The temperature for this transition drops from 445 K in pure clinoatacamite, where no intermediate paratacamite is observed, to room temperature at one-third Zn-occupancy at the interlayer site. This observation shows that Zn or other non-JT-active impurity atoms are the stabilizing factor for paratacamite to develop, by local interruption of the correlation between JT distortions in the interlayer space.

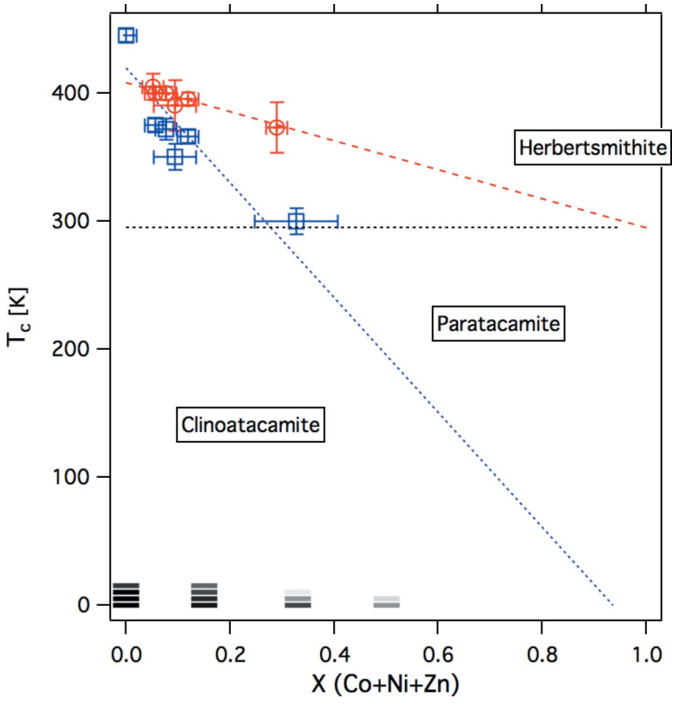

Figure 4
Extrapolated stability fields of clinoatacamite, paratacamite and herbertsmithite as a function of Cu substitution and temperature. The horizontal bars close to 0 K schematically show the static magnetic fraction measured for increasing Zn substitution in synthetic clinoatacamite, as given by Mendels *et al.* (2007). Black indicates 100% frozen fraction and white indicates fully dynamic spin.

Sufficiently short correlation length apparently leads to an ordered distribution of cation sites with a completely dynamic JT distortion, the *M*1 site, and neighbouring cation sites with their JT distortion coupled to the *M*1 sites. For constant concentration of non-JT-active cations, increasing correlation length can be expected with lower temperatures. This will lead to the nucleation of clinoatacamite domains and ultimately the formation of ordered clinoatacamite. For sufficiently high concentrations of non-JT-active cations the correlation length necessary for clinoatacamite to form might not be achieved at all and paratacamite will remain the stable phase, being replaced by fully disordered herbertsmithite at higher temperatures. Fig. 4 shows a provisional phase diagram that is consistent with transition temperatures given by Malcherek *et al.* (2017) and by Welch *et al.* (2014) and with the known transition between monoclinic and trigonal symmetry at room temperature (Jambor *et al.*, 1996). Due to large uncertainties in the transition temperatures, the inferred positions of the boundaries and the overall extension towards ideal herbertsmithite composition are approximate. Nonetheless, there is a clear widening of the ordered paratacamite stability field for intermediate compositions between $Cu_2(OH)_3Cl$ and $Cu_3M(OH)_6Cl_2$. Similarly, the stability field of clinoatacamite might widen at lower temperatures, as the correlation length of the JT distortion can be expected to increase. As clinoatacamite is known to be magnetically ordered at low temperatures, the observation of a frozen magnetic fraction below 10 K for interlayer Zn contents up to 50% (Mendels *et al.*, 2007) might confirm this trend (Fig. 4). Correspondingly, paratacamite may essentially be the stable room-temperature phase for intermediate compositions.

As sufficient interlayer Cu concentrations are required to maintain cooperativeness of the JT displacements, the extension of paratacamite stability towards ideal $Cu_3M(OH)_6Cl_2$ composition, as obtained by linear extrapolation in Fig. 4 is not immediately obvious. Synthetic and natural herbertsmithite type samples with compositions between 0.4 and 1 interlayer Zn *pfu* have been reported, without showing evidence for the superstructure reflections characteristic of paratacamite (Sciberras *et al.*, 2017). On the other hand, paratacamite-(Mg) (Kampf *et al.*, 2013*a*) has been reported with a composition $Cu_3(Mg_{0.6}Cu_{0.4})Cl_2(OH)_6$, not far from the

naturally observed tondiite compositions (Malcherek *et al.*, 2014). Paratacamite-(Ni) (Sciberras *et al.*, 2013) is known with an even lower Cu content, $Cu_3(Ni_{0.7}Cu_{0.3})Cl_2(OH)_6$, placing it well into the stability field shown in Fig. 4.

It is assumed that Zn, Co, Mg or Ni impurities can randomly occupy any interlayer *M* site. Such a non-JT-active ion would not only break the correlation between dynamically JT-distorted sites, but it would also provide an ideal seed for a twin boundary between statically ordered clinoatacamite domains to develop. A strong memory effect for the position of such domain boundaries after cycling through the phase transition to herbertsmithite has been observed in clinoatacamite (Malcherek *et al.*, 2017), providing an indication that the twin boundary positions are indeed fixed by the position of such impurities. Attempts to further substantiate this by element mapping using an electron microprobe did not succeed though, likely caused by insufficient spatial resolution.

5. Kapellasite and haydeeite

The crystal structures of kapellasite (Krause *et al.*, 2006; Colman *et al.*, 2008) and haydeeite (Malcherek & Schlüter, 2007), $Cu_3Zn(OH)_6Cl_2$ and $Cu_3Mg(OH)_6Cl_2$ [Figs. 5(*a*) and 5(*c*)], respectively, derive from those of the isochemical herbertsmithite and tondiite [Figs. 5(*b*) and 5(*d*)] by shifting the interlayer cations Zn or Mg into the vacant octahedral sites of the kagome layers. With the now vacant interlayer sites, this allows stacking of the kagome layers without lateral shift, bonded only by relatively weak O—H···Cl hydrogen bonding. The resulting space group is $P\bar{3}m1$, instead of $R\bar{3}m$ in herbertsmithite. Cu^{2+} cations nominally reside at the 3*e* Wyckoff position, forming a perfect kagome lattice. The Zn or Mg cations should, ideally, reside at the 1*a* site, at the centre of six-membered rings of Cu atoms. As in the herbertsmithite-type compounds, disorder and non-stoichiometry might dilute the presence of Cu cations at the nodes of the kagome lattice, while increasing the probability of paramagnetic Cu at the 1*a* site. In the herbertsmithite-type structures the effect of this disorder is to break the magnetic isolation of individual kagome layers and to distort locally the trigonal structure due to the JT effect. In the kapellasite-type structures, potential Cu at the 1*a* site directly alters the magnetic interactions inside the kagome layers. Kapellasite also differs from herbertsmithite in the Cu—O—Cu bridging angle within the kagome layers, which is about 13° smaller than in herbertsmithite. Consequently the nearest neighbour exchange has been obtained as ferromagnetic, in competition with further neighbour antiferromagnetic interactions (Fåk *et al.*, 2012). For kapellasite, no long-range magnetic order has been found down to temperatures of 20 mK (Fåk *et al.*, 2012; Kermarrec *et al.*, 2014). However, the examined synthetic material is rather deficient in Cu and requires significant Cu/Zn disorder among the 3*e* and 1*a* sites. Even though this disorder and non-stoichiometry does not result in a Cu occupancy of the kagome lattice below the percolation threshold of 0.65 (Kermarrec *et al.*, 2014), it does result in a significant fraction of kagome triangles (5%) entirely occupied by Zn cations, as determined by ^{35}Cl NMR (Kermarrec *et al.*, 2014). Haydeeite appears to be comparatively well ordered regarding distribution of Cu and Mg onto the 3*e* and 1*a* positions, respectively, but it orders ferromagnetically at T_c = 4.2 K (Colman *et al.*, 2010).

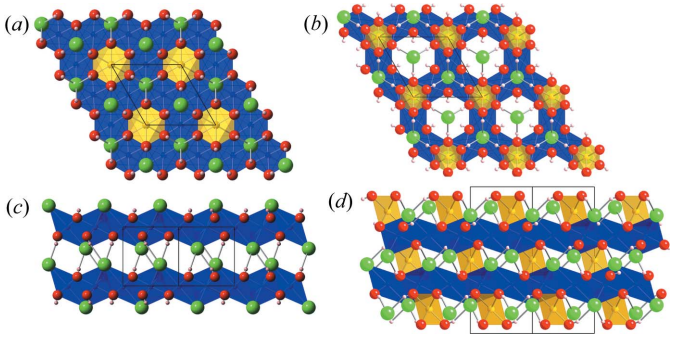

Figure 5
Polyhedral representation of haydeeite (*a*, *c*) and tondiite (*b*, *d*) in projection along [001] (top) and along [110] (bottom). Oxygen atoms are shown in red, Cu in blue, Cl in green and Mg in yellow. Smallest spheres represent hydrogen atoms.

Misakiite, $Cu_3Mn(OH)_6Cl_2$, is isostructural with kapellasite, while centennialite, $Cu_3Ca(OH)_6Cl_2{\cdot}nH_2O$ (Sun *et al.*, 2016; Crichton & Müller, 2017), contains about 0.7 *apfu* molecular water in the interlayer space. The different radii of Ca^{2+} (1.0 Å) and Cu^{2+} (0.77 Å) (Shannon, 1976) support the assumption of little mixing of those cations on the same site, hence a kagome lattice fully occupied by paramagnetic Cu^{2+} cations is expected in centennialite. This has been confirmed by structure refinements on synthetic single crystals (Yoshida *et al.*, 2017). These authors however report a displacement of Ca out of the kagome layers in $Cu_3Ca(OH)_6Cl_2{\cdot}0.6H_2O$, placing Ca on two 1*a* Wyckoff positions in the noncentrosymmetric space group $P3m1$.

6. Future research on minerals within the atacamite family

While the magnetic properties of the atacamite family of minerals and of herbertsmithite in particular have been studied in great detail in recent years, several challenges remain on the way to a perfect experimental kagome antiferromagnet and to the elucidation of its exact ground state. The extent of Cu^{2+}–M^{2+} disorder between the interlayer and kagome layer sites is a key issue as it bears directly on the spin connectivity and coupling of the magnetic lattice, potentially obscuring the true nature of the quantum spin liquid state. A systematic study of the $Cu_3Zn(OH)_6Cl_2$–$Cu_3Mg(OH)_6Cl_2$ series using synthetic samples should give enough X-ray contrast (Mg versus Zn) to allow refinement of meaningful occupancies. Vibrational spectroscopy in the OH-stretching region (2500–3800 cm^{-1}) may also provide information on Cu^{2+}/M^{2+} exchange between interlayer and kagome layer sites for the series. That Raman scattering is very sensitive to the chemical species bonded to the OH group has been shown for the Ni- and Co-containing clinoatacamites studied by Malcherek *et al.* (2017). The significance of recently discov-

ered minerals having M^{2+} = Mn, Co and Ni vis-à-vis spin glasses is worthy of further study, particularly the quantification of magnetic states and properties. More information about the low-temperature structure in mixed crystals of composition $Cu_{4-x}M_x(OH)_6Cl_2$ would help to delineate the transition to clinoatacamite and to further substantiate the true nature of ordered paratacamite. Finally, the presence of dynamic JT distortions in the paratacamite group of minerals opens up orbital degrees of freedom that might couple to the spin system at low temperatures. This possibility has been discussed and contrasted with herbertsmithite for the kagome antiferromagnet vesignieite (Boldrin *et al.*, 2016).

References

Angel, R. J. & Nestola, F. (2016). *Am. Mineral.* **101**, 1036–1045.
Balents, L. (2010). *Nature*, **464**, 199–208.
Boldrin, D., Fåk, B., Enderle, M., Bieri, S., Ollivier, J., Rols, S., Manuel, P. & Wills, A. S. (2015). *Phys. Rev. B*, **91**, 220408.
Boldrin, D., Knight, K. & Wills, A. S. (2016). *J. Mater. Chem. C*, **4**, 10315–10322.
Braithwaite, R. S. W., Mereiter, K., Paar, W. H. & Clark, A. M. (2004). *Mineral. Mag.* **68**, 527–539.
Bramwell, S. T. & Gingras, M. J. P. (2001). *Science*, **294**, 1495–1501.
Burns, P. C. & Hawthorne, F. C. (1996). *Can. Mineral.* **34**, 1089–1105.
Castelnovo, C., Moessner, R. & Sondhi, S. L. (2012). *Annu. Rev. Condens. Matter Phys.* **3**, 35–55.
Colman, R. H., Ritter, C. & Wills, A. S. (2008). *Chem. Mater.* **20**, 6897–6899.
Colman, R. H., Sinclair, A. & Wills, A. S. (2010). *Chem. Mater.* **22**, 5774–5779.
Colman, R. H., Sinclair, A. & Wills, A. S. (2011). *Chem. Mater.* **23**, 1811–1817.
Crichton, W. A. & Müller, H. (2017). *Mineral. Mag.* **81**, 1105–1124.
Fåk, B., Kermarrec, E., Messio, L., Bernu, B., Lhuillier, C., Bert, F., Mendels, P., Koteswararao, B., Bouquet, F., Ollivier, J., Hillier, A. D., Amato, A., Colman, R. H. & Wills, A. S. (2012). *Phys. Rev. Lett.* **109**, 037208.
Fleet, M. E. (1975). *Acta Cryst.* B**31**, 183–187.
Freedman, M. E., Han, T. H., Prodi, A., Müller, P., Huang, Q.-Z., Chen, Y.-S., Webb, S. M., Lee, Y. S., McQueen, T. M. & Nocera, D. G. (2010). *J. Am. Chem. Soc.* **132**, 16185–16190.
Gehring, G. A. & Gehring, K. A. (1975). *Rep. Prog. Phys.* **38**, 1–89.
Grice, J. D., Szymański, J. T. & Jambor, J. L. (1996). *Can. Mineral.* **34**, 73–78.
Han, T. H., Helton, J. S., Chu, S., Nocera, D. G., Rodriguez-Rivera, J. A., Broholm, C. & Lee, Y. S. (2012). *Nature*, **492**, 406–410.
Han, T. H., Helton, J. S., Chu, S., Prodi, A., Singh, D. K., Mazzoli, C., Müller, P., Nocera, D. G. & Lee, Y. S. (2011). *Phys. Rev. B*, **83**, 100402.
Hawthorne, F. C. (1985). *Mineral. Mag.* **49**, 87–89.
Helton, J. S., Matan, K., Shores, M. P., Nytko, E. A., Bartlett, B. M., Yoshida, Y., Takano, Y., Suslov, A., Qiu, Y., Chung, J.-H., Nocera, D. G. & Lee, Y. S. (2007). *Phys. Rev. Lett.* **98**, 107204.
Jambor, J. L., Dutrizac, J. E., Roberts, A. C., Grice, J. D. & Szymański, J. T. (1996). *Can. Mineral.* **34**, 61–72.
Jeschke, H. O., Salvat-Pujol, F. & Valentí, R. (2013). *Phys. Rev. B*, **88**, 075106.
Kampf, A. R., Sciberras, M. J., Leverett, P., Williams, P. A., Malcherek, T., Schlüter, J., Welch, M., Dini, M. & Molina Donoso, A. A. (2013*a*). *Mineral. Mag.* **77**, 3113–3124.
Kampf, A. R., Sciberras, M. J., Williams, P. A., Dini, M. & Molina Donoso, A. A. (2013*b*). *Mineral. Mag.* **77**, 3047–3054.
Kermarrec, E., Mendels, P., Bert, F., Colman, R. H., Wills, A. S., Strobel, P., Bonville, P., Hillier, A. & Amato, A. (2011). *Phys. Rev. B*, **84**, 100401.
Kermarrec, E., Zorko, A., Bert, F., Colman, R. H., Koteswararao, B., Bouquet, F., Bonville, P., Hillier, A., Amato, A., van Tol, J., Ozarowski, A., Wills, A. S. & Mendels, P. (2014). *Phys. Rev. B*, **90**, 205103.
Krause, W., Bernhardt, H.-J., Braithwaite, R. S. W., Kolitsch, U. & Pritchard, R. (2006). *Mineral. Mag.* **70**, 329–340.
Krivovichev, S. V., Hawthorne, F. C. & Williams, P. A. (2017). *Struct. Chem.* **28**, 153–159.
Lee, S.-H., Kikuchi, H., Qiu, Y., Lake, B., Huang, Q., Habicht, K. & Kiefer, K. (2007). *Nat. Mater.* **6**, 853–857.
Lee, S.-H., Takagi, H., Louca, D., Matsuda, M., Ji, S., Ueda, H., Ueda, Y., Katsufuji, T., Chung, J.-H., Park, S., Cheong, S.-W. & Broholm, C. (2010). *J. Phys. Soc. Jpn*, **79**, 011004.
Li, Y.-S. & Zhang, Q.-M. (2013). *J. Phys. Condens. Matter*, **25**, 026003.
Malcherek, T., Bindi, L., Dini, M., Ghiara, M. R., Molina Donoso, A., Nestola, F., Rossi, M. & Schlüter, J. (2014). *Mineral. Mag.* **78**, 583–590.
Malcherek, T., Mihailova, B. & Welch, M. D. (2017). *Phys. Chem. Miner.* **44**, 307–321.
Malcherek, T. & Schlüter, J. (2007). *Acta Cryst.* B**63**, 157–160.
Malcherek, T. & Schlüter, J. (2009). *Acta Cryst.* B**65**, 334–341.
Mendels, P. & Bert, F. (2010). *J. Phys. Soc. Jpn*, **79**, 011001.
Mendels, P. & Bert, F. (2016). *C. R. Phys.* **17**, 455–470.
Mendels, P., Bert, F., de Vries, M. A., Olariu, A., Harrison, A., Duc, F., Trombe, J. C., Lord, J. S., Amato, A. & Baines, C. (2007). *Phys. Rev. Lett.* **98**, 077204.
Nishio-hamane, D., Momma, K., Ohnishi, M., Shimobayashi, N., Miyawaki, R., Tomita, N., Okuma, R., Kampf, A. R. & Minakawa, T. (2017). *Mineral. Mag.* **81**, 485–498.
Norman, M. R. (2016). *Rev. Mod. Phys.* **88**, 041002.
Parise, J. B. & Hyde, B. G. (1986). *Acta Cryst.* C**42**, 1277–1280.
Petříček, V., Dušek, M. & Palatinus, L. (2014). *Z. Kristallogr.* **229**, 345–352.
Pollard, A. M., Thomas, R. G. & Williams, P. A. (1989). *Mineral. Mag.* **53**, 557–563.
Sciberras, M. J., Leverett, P., Williams, P. A., Hibbs, D. E., Downes, P. J., Welch, M. D. & Kampf, A. R. (2013). *Austr. J. Mineral.* **17**, 39–44.
Sciberras, M. J., Leverett, P., Williams, P. A., Schlüter, J., Malcherek, T., Welch, M. D., Downes, P. J., Hibbs, D. E. & Kampf, A. R. (2017). *Mineral. Mag.* **81**, 123–134.
Scott, D. A. (2000). *Stud. Conserv.* **45**, 39–53.
Shannon, R. D. (1976). *Acta Cryst.* A**32**, 751–767.
Shores, M. P., Nytko, E. A., Bartlett, B. M. & Nocera, D. G. (2005). *J. Am. Chem. Soc.* **127**, 13462–13463.
Sun, W., Huang, Y.-X., Pan, Y. & Mi, J.-X. (2016). *Phys. Chem. Miner.* **43**, 127–136.
Vries, M. A. de, Stewart, J. R., Deen, P. P., Piatek, J. O., Nilsen, G. J., Rønnow, H. M. & Harrison, A. (2009). *Phys. Rev. Lett.* **103**, 237201.
Vries, M. A. de, Wulferding, D., Lemmens, P., Lord, J., Harrison, A., Bonville, P., Bert, F. & Mendels, P. (2012). *Phys. Rev. B*, **85**, 014422.
Welch, M. D., Sciberras, M. J., Williams, P. A., Leverett, P., Schlüter, J. & Malcherek, T. (2014). *Phys. Chem. Miner.* **41**, 33–48.
Wills, A. S. & Henry, J.-Y. (2008). *J. Phys. Condens. Matter*, **20**, 472206.
Yang, H., Barton, I. F., Andrade, M. B. & Downs, R. T. (2016). *Am. Mineral.* **101**, 986–990.
Yoshida, H., Noguchi, N., Matsushita, Y., Ishii, Y., Ihara, Y., Oda, M., Okabe, H., Yamashita, S., Nakazawa, Y., Takata, A., Kida, T., Narumi, Y. & Hagiwara, M. (2017). *J. Phys. Soc. Jpn*, **86**, 033704.
Zheng, X. G., Mori, T., Nishiyama, K., Higemoto, W., Yamada, H., Nishikubo, K. & Xu, C. N. (2005). *Phys. Rev. B*, **71**, 174404.
Zhou, Y., Kanoda, K. & Ng, T.-K. (2017). *Rev. Mod. Phys.* **89**, 025003.